

Nanoindentation and scratch resistance of multilayered TiO₂-SiO₂ coatings

Nanoindentation and scratch resistance of multilayered TiO₂-SiO₂ coatings with different nanocolumnar structures deposited by PV-OAD

J J Roa^{1,2,*}, V Rico³, M Oliva-Ramírez³, A R González-Elipe³ and E Jiménez-Piqué^{1,2}

¹ CIEFMA - Departament de Ciència dels Materials i Enginyeria Metal·lúrgica, ETSEIB, Universitat Politècnica de Catalunya, Avda. Diagonal 647 08028 Barcelona, Spain

² CRnE, Campus Diagonal Sud, Edificio C', Universitat Politècnica de Catalunya, C. Pascual i Vila 15, 08028 Barcelona, Spain

³ Instituto de Ciencia de Materiales de Sevilla (CSIC-Univ. Sevilla), Avda. Américo Vespucio 49, 41092 Sevilla, Spain

* E-mail: corresponding autor joan.josep.roa@upc.edu

Abstract. This paper presents a study of the mechanical properties and an evaluation of damage mechanisms of nanocolumnar TiO₂-SiO₂ multilayer coatings prepared by physical vapour oblique angle deposition at different configurations (slanted, zigzag or chiral) and two zenithal evaporation angles (70° or 85°). The characterization at micro- and nano-metric length scales of the mechanical properties of the multilayers has been carried out by nanoindentation and nanoscratch tests, while the morphological evaluation the surface and sub-surface damages produced with a sharp indenter and the adhesive and/or cohesive failures between coating and substrate have been investigated by field emission scanning electron microscopy and focused ion beam, respectively. The obtained results have shown that the main processing parameters controlling the mechanical response of the different multilayers is the zenithal angle of deposition and the number of layers in the multilayer stack, while the coating architecture had only a minor effect on the mechanical response. This analysis also revealed a higher resistance to scratch testing and a brittle failure behaviour for the low zenithal angle coatings as compared with the high angle ones.

Keywords: TiO₂-SiO₂ coatings; multilayer thin films; oblique angle deposition; glancing angle deposition; nanoindentation; nanoscratch; fracture mechanism.

1. Introduction

Due to their outstanding optical, photoactive or protective properties, TiO₂-SiO₂ multilayer coatings are widely used for a large set of applications [1], where the micromechanical properties of the coatings in terms of hardness, elastic modulus and interfacial cohesion and/or adhesion with the substrate are key issues to assure the structural integrity and reliability of the components [1]. Mechanical stability is even more critical for nanostructured coating systems prepared by physical vapour oblique angle deposition (PV-OAD), also known with the term glancing angle deposition (GLAD) [2,3]. These nanocolumnar structures can be prepared in a wide range of architectures changing the zenithal angle of evaporation and rotationally moving the substrate during deposition [4,5]). In our group, TiO₂-SiO₂ multilayer nanocolumnar

systems behaving as 1D photonic crystals or Bragg microcavities have been used for liquid sensing applications [6,7]. Applications as polarized light emitters, selective transmitters or humidity sensors have been reported by others [8,9,10]. However, mechanical properties such as hardness, elastic modulus or interfacial cohesion of this type of nanostructured multilayer TiO₂-SiO₂ coatings have not been reported so far. In previous works, the mechanical properties of TiO₂ nanocolumnar coatings made by PV-OAD were investigated as a function of the zenithal angle of deposition [19,21], finding a strong dependence between the mechanical response and the deposition angle. The objective of the present work is to characterize the mechanical response of multilayer coatings formed by a different number layers of TiO₂ and SiO₂ stacked in the form of distinct microarchitectures where the tilted nanocolumns in successive layers present slanted, zigzag or chiral configurations. To assess the mechanical behavior of these multilayers and to assess their mechanical integrity, herein we have carried out a systematic nanoindentation study using different indenter tip geometries and contact loading conditions (i.e. indentation/scratch) [11,12,13,14,15,16] and applying the well-established Oliver and Pharr method of data analysis [17]. Special attention has been also paid to analyse the main damage and fracture events at micro- and nanometric length scales affecting both the whole layer assemblage and the coating/substrate interface as a function of the coating architecture. For this purpose, field emission scanning electron microscopy (FESEM) has been used to analyse the effect of the indenter on the coating integrity under scratch testing, while focused ion beam (FIB) has served to cross-sectioning the sub-surface damage zones induced under sliding contact tests and thus deduce basic features of the cohesive/adhesive failure mechanisms involved.

2. Experimental procedure

2.1. Coating deposition

Nanostructured multilayer coatings consisting of three and seven successive and alternant layers of TiO₂-SiO₂ have been prepared by electron beam evaporation of these two materials at zenithal deposition angles of 70° and 85° between the crucible position and the perpendicular to the substrates. The thickness of each single layer was adjusted at approximately 85 nm. Details about the deposition procedure and conditions can be found elsewhere [7]. While performing the deposition, the substrate was maintained fixed or azimuthally turned by 180° or 90° when passing from one layer to the next. These deposition conditions gave rise to slanted (S), zigzag (Z) and chiral (C) configurations where the tilted nanocolumns forming the basic microstructure of PV-OAD films arranged according to these architectures in the multilayer stack.

Table 1 summarizes the labels used, deposition glancing angle, microarchitecture as well as the thickness of the different coatings under study.

Table 1. Sample labelling, deposition glancing angle, number of kinks and thickness.

Label	Number of layers	Zenithal angle of deposition (°)	Mircoarchitecture ^a	Thickness, <i>t</i> (nm) ^b
3 70 S	3	70	S	255
3 70 Z			Z	
3 70 C			C	
3 85 S	3	85	S	255
3 85 Z			Z	
3 85 C			C	
7 70 S	7	70	S	595
7 70 Z			Z	
7 70 C			C	
7 85 S	7	85	S	595
7 85 Z			Z	
7 85 C			C	

^a S: slanted, Z: zigzag, and C: chiral

^b All the coating systems presents a constant bilayer period equals to 170 nm

Figure 1 shows, for the case of seven stacked layers, a series of cross section FESEM micrographs of these multilayer coating films where it is clearly appreciable the different configurations of the tilted nanocolumns and the transition from one layer to next, this latter evidenced by the different brightness zones in the image. The schemes included in the figure clarify this different orientation of nanocolumns between one layer and the next.

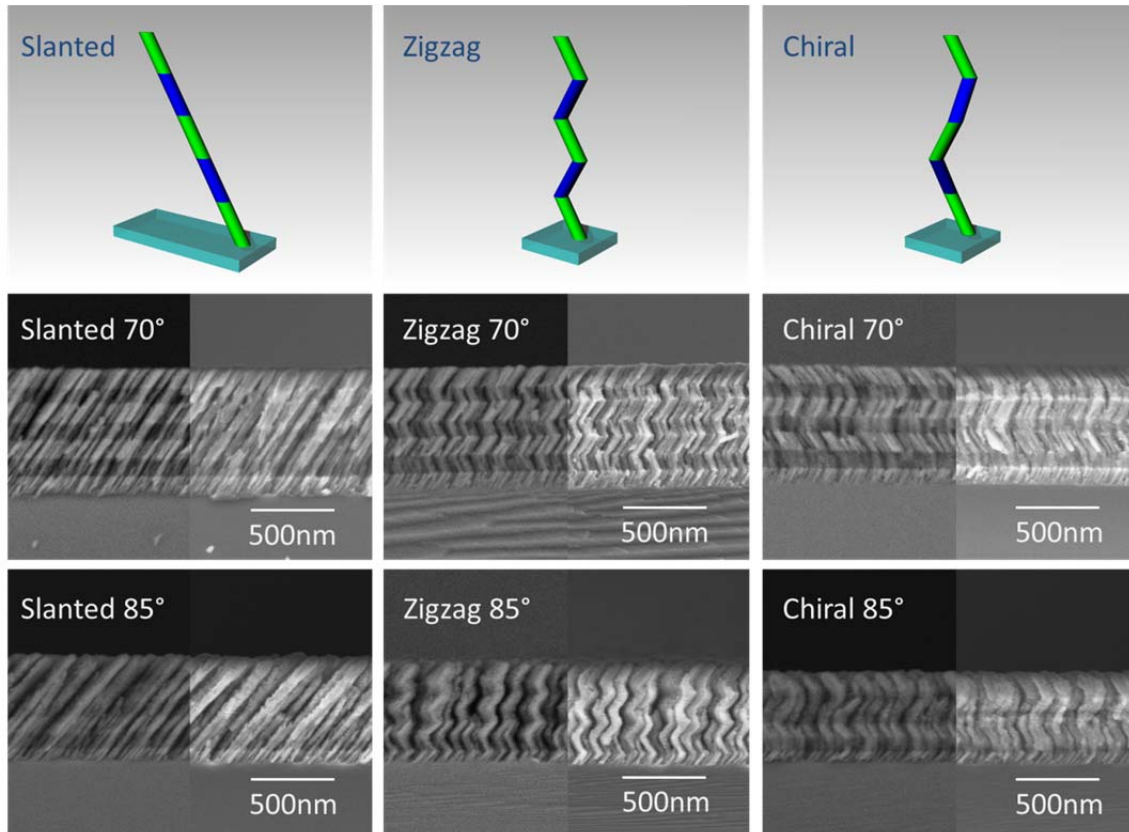


Figure 1. Schemes with the arrangement of nanocolumns in the successive stacked layers and SEM cross section micrographs (left part is observed on backscattered electron image while in the right part is observed on secondary electron imaging) of the slanted, zigzag and chiral seven multilayer structures prepared by oblique angle deposition at 70° and 85°, as indicated.

2.2. Mechanical integrity

The different coatings were mechanically evaluated using a Nanoindenter XP from MTS, equipped with a continuous stiffness measurement (CSM) module, allowing the dynamic determination of the mechanical properties along the indentation process [18]. Tests were done with a Berkovich tip calibrated against a fused silica standard at a constant strain rate of 0.05 s⁻¹. A regularly spaced array of 16 imprints (4 by 4) was done for each sample until a maximum penetration depth of 500 nm, and results were averaged for all measurements. Hardness (*H*) and elastic modulus (*E*) values were determined by the Oliver and Pharr method [17]. In addition, to directly extract the true hardness and elastic modulus of each coating, hardness was directly determined at a penetration depth equal to 10% of the coating thickness, and analytical or were used to deconvolute the elastic modulus of the coating.

Sliding contact tests were done at a micrometer length scale by means of a nanoscratch fixture attached to the nanoindenter system referred above. A Berkovich indenter was employed to scratch at a velocity of 10 μm/s the different coating under increasing load, up to a maximum of 50 mN. Different scan tracks were done on each specimen at a fixed distance between tracks of 200 μm.

2.3. Damage and fracture assessment

The surface damage associated with residual nanoindentation imprints and sliding tracks were visualized by field emission scanning electron microscopy at 20 kV (FESEM, JEOL 7100 F). The subsurface damage induced during indentation and scratch tests was inspected by means of focused ion beam (FIB). Cross-sectioning and microscopy was conducted in a dual beam Workstation (Zeiss Neon 40). A thin platinum layer was deposited on the sample prior to milling with the aim of reducing ion-beam damage. A Ga⁺ ion source was used to mill the surface at a voltage of 30 kV. The final polishing of the cross-section was performed at a current of 200 pA.

3. Results and discussion

3.1. Hardness and elastic modulus

The variation of indentation hardness and elastic modulus as a function of penetration depth is reported in **Figures 2**. The plots in these figures evidence a clear influence of the deposition angle on the mechanical response of the coatings, but no significant effect of the type of microstructure. A similar behaviour has been previously found for TiO₂ coatings [19] where, similarly to the multilayer system investigated here, the zenithal angle of deposition was the main parameter determining their mechanical properties. In this kind of analysis, at large penetration depths, when the plastic and elastic fields are not confined inside the coating, the mechanical properties are affected by the substrate. The increase in the apparent values of both indentation hardness and elastic modulus clearly observed in Figure 2 must be associated to the harder and stiffer nature of the silica substrate employed in this investigation. Substrate affections of the mechanical properties measurements of coatings can be suppressed by limiting the indenter penetration to 10% of thickness only to extract the intrinsic hardness of the coating without any surface influence, while in order to extract reliable values of the elastic modulus of the coatings have been obtained using the model proposed by Bec et al [20] to deconvolute the Young's modulus curves. In this model, the dependence of elastic modulus (E) on penetration is taken as follows:

$$\frac{1}{E_{eff}} = \frac{2 \cdot a}{1 + \frac{2 \cdot t}{\pi \cdot a}} \left(\frac{t}{\pi \cdot a^2 \cdot E_f} + \frac{1}{2 \cdot a \cdot E_s} \right) \quad (1)$$

where E_{eff} is the effective elastic modulus determined through the equation proposed by Oliver and Pharr [17], the subindexes f and s refer to film and substrate, respectively, a is the contact radius, and t is the thickness of the coating. The Poisson coefficient is kept constant to 0.25 for all the specimens investigated here.

Nanoindentation and scratch resistance of multilayered TiO₂-SiO₂ coatings

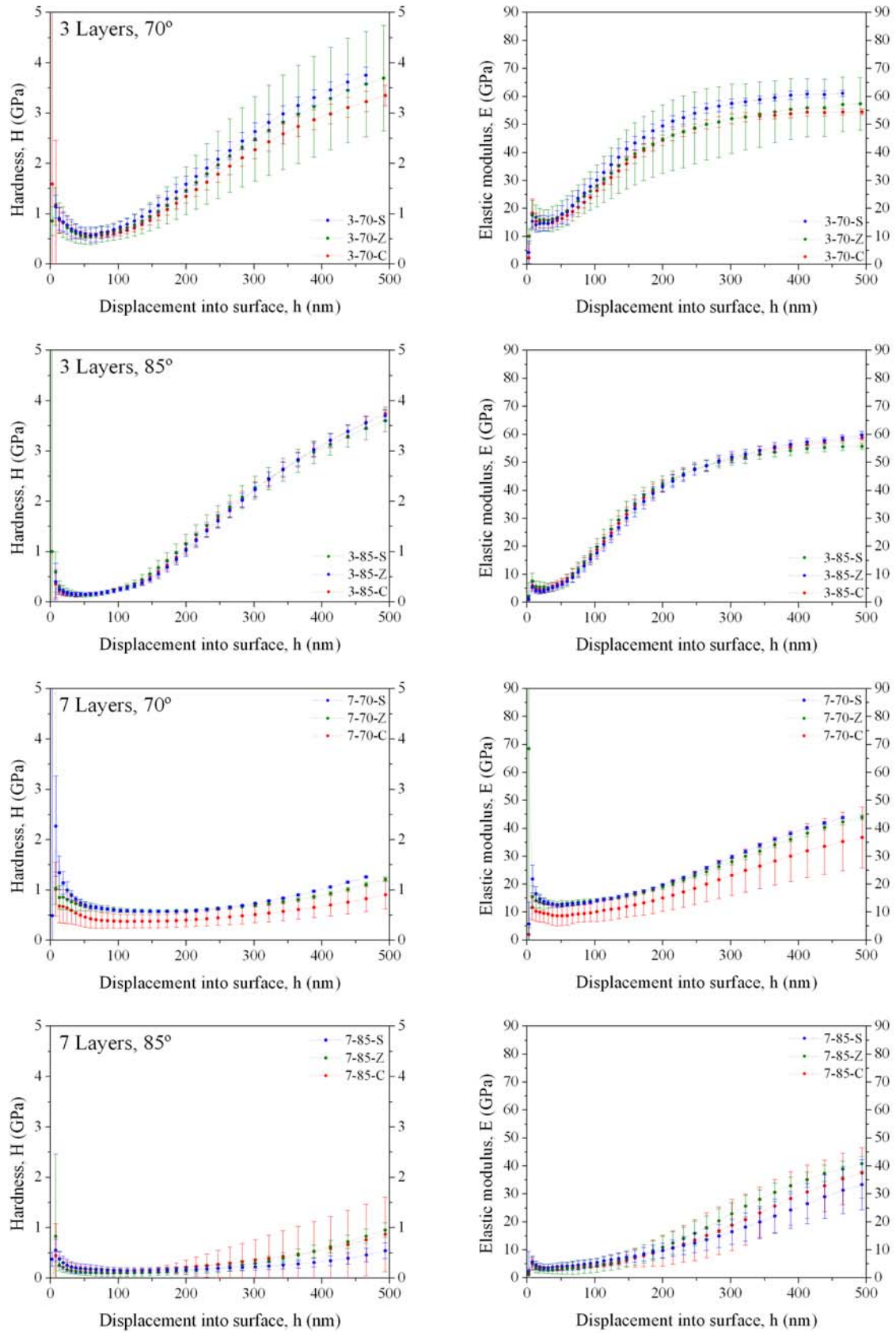


Figure 2. Mechanical properties for the indicated coated systems as a function of zenithal angle of deposition (70° and 85°), microstructure (S : slanted; Z : zigzagged and C : chiral) and number of layers (3 and 7) as a function of the displacement into the films. Hardness (left hand) and Elastic modulus (right hand).

Table 2 summarizes the values of hardness and elastic modulus calculated according to both the 10% rule and the Bec et al. [20] model. The hardness data presents a relatively large scatter due to the heterogeneity of the coating in terms of local variation in column geometry and porosity. These data are also presented in **Figure 3a and b**, in order to better compare the different values of hardness and elastic modulus, respectively.

Table 2. Hardness (*H*) and elastic modulus (*E*) extracted by nanoindentation for the different coatings investigated here using the 10% rule and the deconvolution of the indentation elastic modulus through the Bec *et al.* model [20], respectively. *S*: slanted, *Z*: zigzagged and *C*: chiral.

Number of layers	Deposition Angle	Micro-architecture	Label	<i>H</i> (MPa)	<i>E</i> (GPa)
3	70°	S	3 70 S	645 ± 307	11.7 ± 4.3
		Z	3 70 Z	778 ± 176	12.7 ± 3.5
		C	3 70 C	725 ± 242	15.8 ± 3.9
	85°	S	3 85 S	158 ± 47	5.1 ± 1.3
		Z	3 85 Z	175 ± 47	4.6 ± 0.9
		C	3 85 C	193 ± 78	4.9 ± 1.9
7	70°	S	7 70 S	430 ± 182	11.7 ± 4.3
		Z	7 70 Z	675 ± 48	21.9 ± 5.0
		C	7 70 C	662 ± 86	15.4 ± 3.9
	85°	S	7 85 S	177 ± 45	4.9 ± 1.9
		Z	7 85 Z	180 ± 87	5.8 ± 1.7
		C	7 85 C	114 ± 65	5.3 ± 2.6

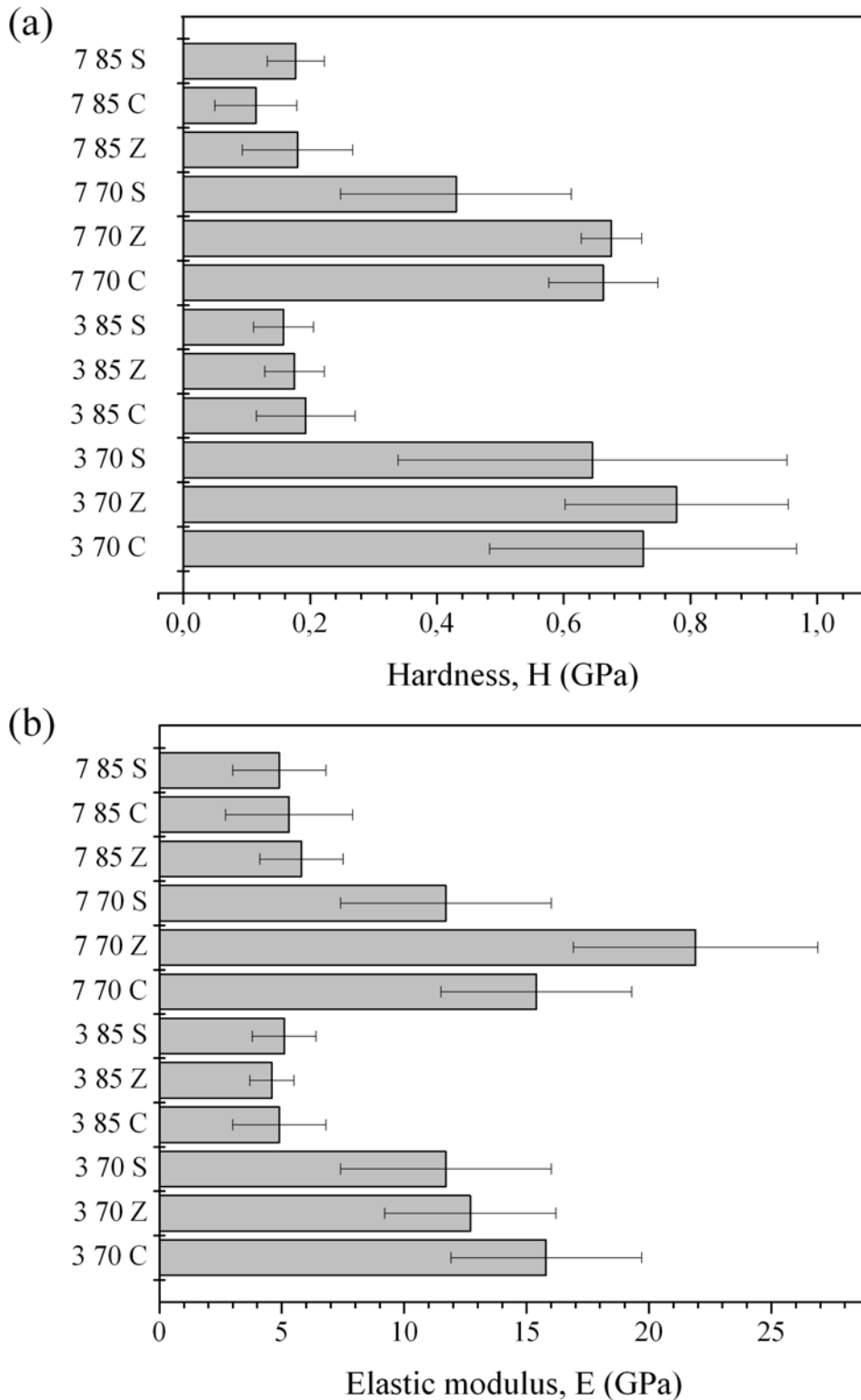


Figure 3. Hardness (a) and elastic modulus (b) bar diagrams of the different investigated samples.

This figure clearly shows that hardness and elastic modulus depend on the deposition angle, a result that agrees with previous results for TiO₂ PV-OAD coatings [19,21]. Common features of PV-OAD thin films, including the TiO₂-SiO₂ multilayers studied here, are that both the tilting angle of nanocolumns and the void space increase with the deposition angle (c.f., **Figure 1**)

[2,3,6,7]. This is also the case for multilayer coatings as can be evidenced in the FESEM micrographs of the slanted microstructure in **Figure 1**, where an increase in the tilting angle of nanocolumns from about 30° to 45° can be appreciated when examining the micrographs of the 70° and 85° samples, respectively. We attribute to the combination of these two morphological features the fact that the stiffness in the normal direction and the E and H values are lower for the higher zenithal angle coatings. Unlike this dependence on the deposition angle, other morphological features such as number of layers and stacked layer configuration appear to have a negligible influence on the nanoindentation response. A plausible explanation for this invariance is that even for low indenter penetration depths of around 100 nm, this value is already larger than the individual layer thickness (i.e., around 75nm) and therefore the measured convolution of the mechanical responses of the two materials render no differences between 3 or 7 stacked layers coatings. Moreover, for shallower penetration depths, surface effects, especially roughness, would make the measurements unreliable.

The microarchitecture of the coatings (i.e., slanted, zigzag or chiral configurations) also appears to have a small influence on the nanoindentation response. We attribute, this invariance to the averaging of the individual nanocolumnar features in each layer of the coating within the total and much larger volume of the nanoindentation imprint.

3.2. Sliding contact analysis and damage events

Due to their larger thickness and superior structural integrity, studies on possible relationships between coating microarchitecture and scratch resistance were carried out with the 7 layers samples deposited at 70°. **Figure 4** shows a series of top-view FESEM images of the nanoscratch tracks produced on samples with chiral, zigzag and slanted microstructures. During scratch, all samples presented similar resistance to penetration depth. Furthermore, a common feature in these micrographs is the appearance of several damage events (like microcracks and spalling) at the track sides.

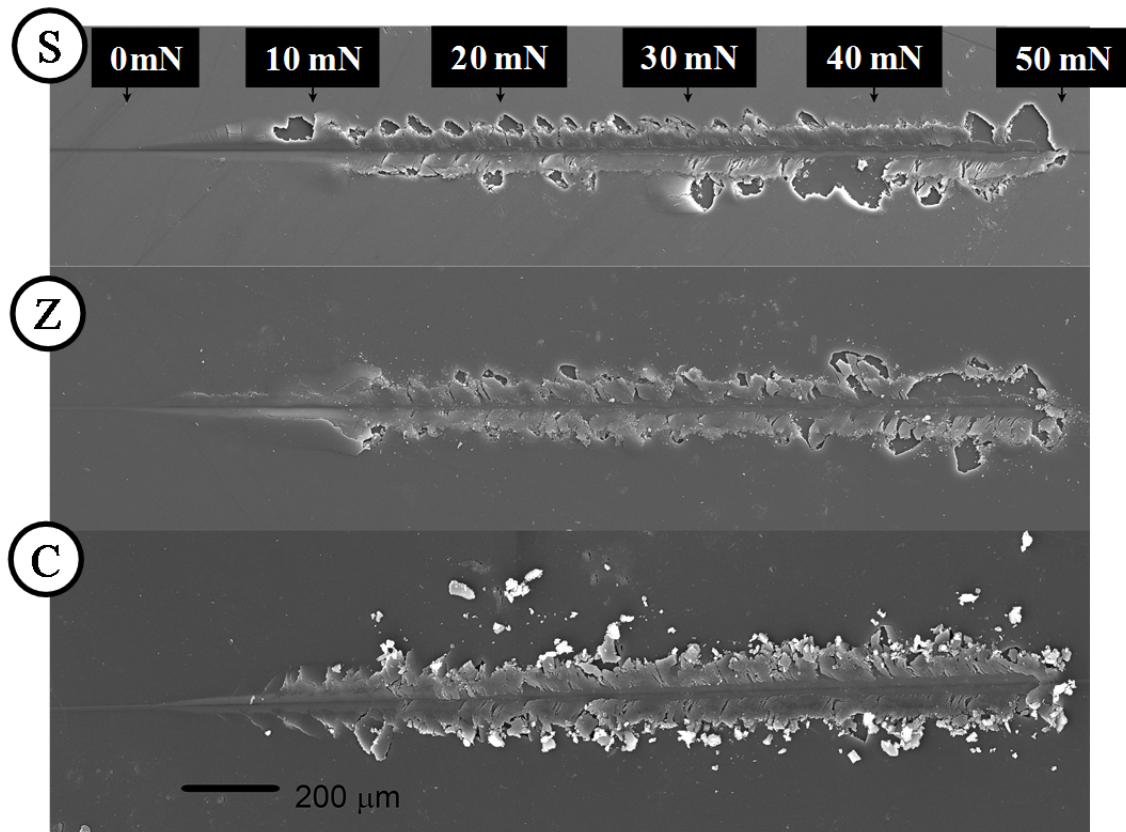


Figure 4. Top-view FESEM images along the nanoscratch tracks (from 0 up to 50 mN of maximum applied load) for the 7 layer 70° specimens of different coating microstructure as indicated showing damage tracks induced in each case.

Damage, appearing at low applied loads (5mN) can be attributed to a combination of delamination and radial cracking mechanisms [22,23,24,25] that differed depending on sample microstructure. Thus, delamination predominated in sample C, radial cracking in sample S and an intermediate behaviour was found in sample Z, with surface damage appearing at slightly higher load values than in the two other coating types. At higher loads, the two types of damage were evident in the three types of coatings, although the delamination degree was higher for sample C than in the other two samples. To get a better insight of the interfacial fracture mechanisms, several FIB cross-sections were acquired at the position where a 37.5 mN scratch load was applied (i.e., corresponding to a scratch length of around 150 μm). **Figure 5** evidences that damage deformation is mainly located within the coating, without any influence of the substrate. Samples C and Z present a similar damage behaviour, consisting of a neat delamination from the substrate, some interlayer delamination and a considerable cracking specially in the zones of maximum curvature. This cracking suggests that the damage may have been produced to accommodate the coating buckling. Unlike these two samples, coating S depicts smaller delamination area accompanied by a quite wider coating cracking. These differences in mechanical response can be rationalized in terms of the different microarchitectures of the coatings. Sample S is made of straight slanted columns which makes the crack propagation easier, while samples C and Z are composed of twisted columns that will interfere with the crack growth. Therefore, in samples C and Z the loading induces a deformation that extends through the whole coating and ultimately lead to cracking due to strain accumulation. As a result, S coatings are more brittle and their fracture easier, while C and Z coatings are able to accommodate the scratch loading deformations by buckling and delamination, leading to cracking in the regions of maximum strain.

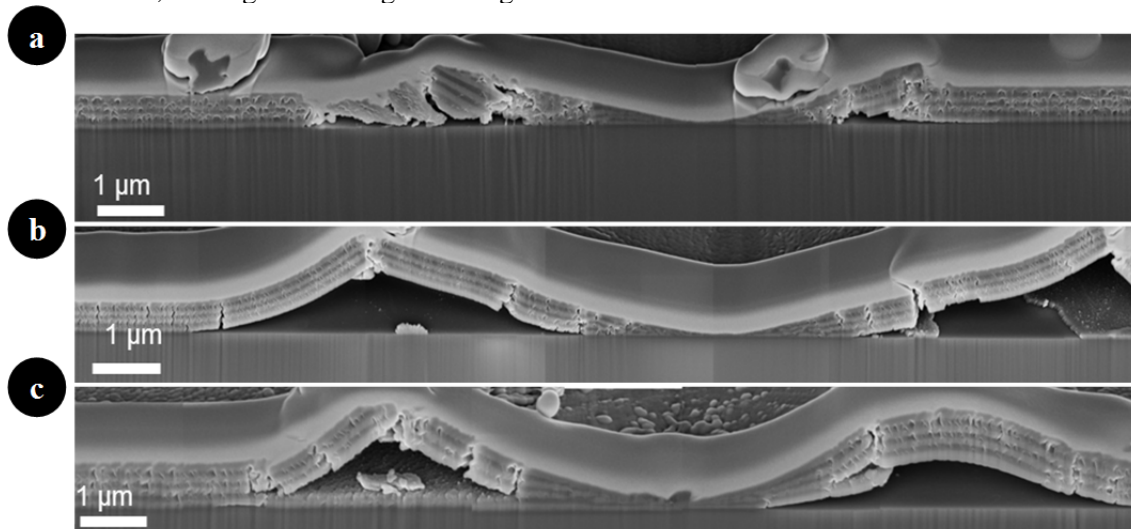


Figure 5. High magnification FIB cross-section images perpendicular to sliding direction using a Berkovich indenter for the whole set of specimens labelled in **Table 1** as 7-70, showing the microstructural changes at the subsurface, along the nanoscratch track (applied normal load of 37.5 mN, which corresponds to a scratch length of around 150 μm) for (a) S, (b) Z, (c) C.

4. Conclusions

In this study we have characterized the mechanical stability and damage behaviour of TiO₂-SiO₂ PV-OAD coatings under different stress fields in order to determine their mechanical properties (i.e. hardness and elastic modulus). In addition, we have studied the different damage scenarios under sliding contact. From the analysis of the experimental results, the following conclusions have been drawn:

- i) The main processing parameter controlling the mechanical response of the coatings is the zenithal deposition angle. Other features such as the layer architecture and number of layers play a minor role.

- ii) Critical load for all the coating systems is around 5 mN. Cohesive damage in microscratch testing by using a sharp Berkovich indenter tip is independent of the coating microstructure. Interfacial decohesion is observed for the TiO₂-SiO₂ coatings with chiral and zigzag microstructures, while for the slanted coatings large microcracking can be appreciated around the edge of the sliding tracks.

Acknowledgements

The authors greatly acknowledge I. López from the “Laboratori de Microscopi Electrònica del CMEM-UPC” for his contribution to the FESEM measurements. Furthermore, we would like to thank the support received from Direcció General de Recerca del Comissionat per a Universitats i Recerca de la Generalitat de Catalunya through recognition of CIEFMA as Grup de Recerca Consolidat (2014-SGR-130) and the MINECO (projects MAT2013-40852-R and RECUPERA 2020, this latter co-funded with structural funds of the EU). Dr. J.J.Roa would like to thank the Juan de la Cierva Programme for its financial support (grant number: JCI-2012-14454).

References

-
- [1] Martinu L and Poitras D 2000 *J. Vac. Sci. Technol. A* **18** 2619
 - [2] Hawkeye M M, Taschuk M T and Brett M J 2014 *Glancing Angle Deposition of Thin Films*. John Wiley & Sons, Ltd
 - [3] Barranco A, Borrás A R, Gonzalez-Elipe A and Palmero A 2015 *Progr. in Mater. Sci.* (DOI 10.1016/j.pmatsci.2015.06.003)
 - [4] Van Popta A C, Cheng J, Silt J C and Brett M J 2007 *J. Appl. Phys.* **102** 013517
 - [5] Hawkeye M M and Brett M J 2007 *J. Vac. Sci. Technol. A* **25** 1317
 - [6] González-García L, Lozano G, Barranco A, Míguez H and González-Elipe A R 2010 *J. Mater. Chem.* **20** 6408
 - [7] Oliva-Ramirez M, Gonzalez-Garcia L, Parra-Barranco J, Yubero F, Barranco A and Gonzalez-Elipe A R 2013 *ACS Appl. Mater. Interfaces* **5** 6743.
 - [8] Gospodyn J, Taschuk M T, Hrudehy P C, Tsui Y Y, Fedosejevs R, Brett M J and Sit J C 2008 *Appl. Opt.* **47** 2798
 - [9] Leontyev V, Wakefield N G, Tabunshchyk K, Sit J C, Brett M J and Kovalenko A 2008 *J. Appl. Phys.* **104** 104302
 - [10] Liu Y J, Shi J, Zhang F, Liang H, Xu J, Lakhtakia A, Fonash S J and Huang T J 2011 *Sens. Actuators B Chem.* **156** 593
 - [11] Shetty A R, Karimi A and Cantoni M 2011 *Thin Solid Films* **519** 4262
 - [12] Horwat D, Jiménez-Piqué E, Pierson J F, Migot S, Dehmas M, Anglada M 2012 *J. Phys. Chem. Solids* **73** 554
 - [13] Roa J J, Jiménez-Piqué E, Puig T, Obradors X and Segarra M 2011 *Thin Solid Films* **519** 2470
 - [14] Yalamanchili K, Forsén R, Jiménez-Piqué E, Johansson Jöessar M P, Roa J J, Ghafoor N and Odén M 2014 *Surf. Coat. Technol.* **258** 1100
 - [15] Roa J J, Gilioli E, Bissoli F, Pattini F, Rampino S, Capdevila X G and Segarra M 2009 *Thin Solid Films* **518** 227
 - [16] Ballarre J, Jiménez-Piqué E, Anglada M, Pellice S and Cavalleri A L 2009 *Surf. Coat. Technol.* **203** 3325.
 - [17] Oliver W C and Pharr G M 1992 *J. Mater. Res.* **7** 1564
 - [18] Oliver W C and Pharr G M 2004 *J. Mater. Res.* **19** 3
 - [19] Jiménez-Piqué E, González-García L, Rico V J and González-Elipe A R 2014 *Thin Solid Films* **550** 444
 - [20] Bec S, Tronck A and Loubet J L 2006 *Philos. Mag.* **86** 5347
 - [21] Gaillard Y, Rico V J, Jiménez-Piqué E and González-Elipe A R 2009 *J Phys D: Appl. Phys.* **42** 145305/1
 - [22] Diao G M, Kato K and Hokkirigawa K 1994 *J. Tribol. –Trans. ASME* **116** 860

- [23] Hamilton G M and Goodman L E 1976 *J. Appl. Mech.* **88** 371
- [24] Lawn B 1967 *Proc. Royal Soc. Of London A.* **299** 307
- [25] Hamilton G M 1983 *Proc. Ins. Mech. Eng.* **197C** 53